New Explorations in Electrical Engineering (NECE)
Department of Electrical Engineering,
Faculty of Engineering
Universiti Malaya, MALAYSIA

Vol. 1, No. 2 (2025)
pp. 69–89

ResNet-Based Downscaling of ERA5 Wind Data for Enhanced Wind Resource Assessment in Ambon Island, Indonesia

Wahyu Sri Bimantoro[a]*, Noraisyah Mohamed Shah[b] and Mohammad Omar Faheem[b]

[a]*Indonesian Meteorology Climatology, and Geophysical Agency, Jakarta 10610, Indonesia*

[b]*Department of Electrical Engineering, Faculty of Engineering, Universiti Malaya 50603 Kuala Lumpur Malaysia*

Corresponding e-mail: wahyu.sri@bmkg.go.id

Abstract. Accurate wind resource assessment in complex island topographies demands high-resolution spatial datasets that conventional 31-km reanalysis products fail to capture. An advanced encoder-decoder Residual Neural Network (ResNet) framework is developed to spatially downscale ERA5 wind fields to a 1-km grid over Ambon Island, Indonesia. The proposed architecture combines geostatistical kriging with deep residual learning and multi-channel inputs of ERA5 atmospheric profiles and SRTM digital elevation data, and relies solely on independent ground observations for validation. Validation reveals a clear spatial trade-off: classical baselines tend to overfit local inland anomalies, whereas the ResNet architecture exhibits better spatial generalization over complex coastal-to-marine transition zones, with a Mean Absolute Error (MAE) of 2.17 m/s at the variable 10-m surface layer, representing a 54% error reduction with respect to raw ERA5 data. Extrapolated to a 100-m hub height, where surface friction diminishes, the architecture successfully isolates high-potential wind corridors along the southern Leitimur peninsula (4.5–7.5 m/s). While localized overestimation in built-up grids highlights the limits of pure elevation-driven downscaling without dynamic surface roughness (z_0) inputs, the architecture effectively captures macro-topographic wind acceleration. This framework offers a scalable, transferable methodology for wind mapping in data-sparse, topographically complex archipelagic environments.

Keywords. Ambon Island, ERA5 reanalysis, ResNet, Spatial downscaling, Wind resource assessment

1. Introduction

Territorial fragmentation and rugged coastal topographies are key drivers of the microclimate of equatorial archipelagos, thus local wind resource assessments are a logistic bottleneck rather than a standard analytical exercise. While new regional frameworks increasingly depend on wind energy generation to achieve sustainability goals (Ángel-Sanint et al., 2023), performing viable microgrid infrastructure planning over these complex terrains is still heavily bottlenecked by spatial data limitations. The root of this issue lies in a severe scale mismatch, as standard global reanalysis products operating at a coarse 31-km grid resolution mathematically smooth out the sharp terrain-wind interactions, land-sea breeze boundaries, and localized flow accelerations that govern actual energy yields (Hersbach et al., 2020). Consequently, generating high-fidelity wind maps for isolated, topographically complex configurations—such as Ambon Island, Indonesia—presents a distinct computational challenge that conventional interpolation methods fail to resolve.

In the case of sparse in-situ measurements, gridded products are the main source of macro-scale atmospheric fields. The ECMWF reanalysis platform, ERA5, provides continuous, multi-decadal atmospheric datasets over global domains (Hersbach et al., 2020). The platform captures synoptic-scale circulations as well as regional pressure gradients (Kalverla et al., 2019). However, its 31-km grid spacing creates an immediate bottleneck over small islands. Rugged topographies are mathematically averaged into flat grid cells. This spatial smoothing leads to significant data discrepancies along complex coastlines, where sharp land-sea thermal boundaries and rapid elevation changes actually govern near-surface wind patterns.

Resolving this scale mismatch traditionally involves Numerical Weather Prediction (NWP) models to dynamically downscale coarse data across nested grids. While physically accurate, high-resolution NWP runs are too computationally expensive for multi-year local studies. On a statistical level, geostatistical methods like universal kriging offer a faster alternative. These approaches disaggregate larger reanalysis cells in space by adding elevation proxies (Luo et al., 2008). However, linear interpolation is not well suited to disentangle highly non-linear interactions between moving air masses and steep mountain slopes. To overcome these shortcomings, deep learning networks are being deployed at an increasing rate. These structures are well suited to model complex wind-terrain feedbacks, providing accurate spatial mapping across complex environments at a fraction of the computational cost needed by purely physical models (Höhlein et al., 2020; Veronesi et al., 2016).

Geographically, the province of Maluku is a microcosm of the major challenges behind energy distribution in archipelagic contexts. The province consists of 1,340 islands with water covering an area of around 92.4% of the region and land only 7.6%. The area suffers from acute deficits in grid infrastructure, with 34% of villages lacking electricity access as of 2017 (Pelupessy & Manuhutu, 2019). Wind patterns of this maritime zone are dictated by rigid monsoonal cycles with baseline speeds of 3–4 m/s in sheltered areas and over 5 m/s in optimized areas at 50 meters above ground level (Pelupessy & Manuhutu, 2019). The cut-in wind speed of 3-5 m/s is common for modern turbines, but for economic viability in the long term, a continuous wind speed of 6-8 m/s is generally required (Deng et al., 2015; Langer et al., 2022). The meteorological data from the Pattimura Ambon Meteorological Station show a monthly average wind speed of 4.0 m/s and short-term maximum speeds of up to 7.5 m/s (Statistics, 2024). These resources are defined by a substantial variability across the island's geography with coastal areas experiencing stronger and more stable flow patterns than the mountainous interior.

Initial assessments of the regional energy matrix identified wind flows as a potential but underutilized resource, with the main obstacles being major terrain barriers (Pambudi et al., 2023; Shafira et al., 2023). A dedicated empirical study of Ambon Island found extreme spatial variation in wind energy potential, with coastal fronts having the highest generation metrics but also erratic diurnal cycles not captured by standard macroscale models (Nunumete, 2015). Numerical simulations with the Weather Research and Forecasting (WRF) model were recently employed to characterize Ambon's wind streams at a 3-km grid resolution (Cendrawati et al., 2023). However, dynamic downscaling using NWP models such as WRF is computationally infeasible for multi-decadal resource assessments, and a 3-km resolution remains too coarse to resolve important sub-grid aerodynamic effects from Ambon's complex micro-scale ridges.

Atmospheric motion operates under extreme spatial and temporal volatility, meaning any infrastructure planning data must rely on highly precise localized scaling (Sørensen et al., 2018). While dense networks of surface weather stations can supply this granularity, the sparse layout of physical observatories in developing island regions leaves massive data voids. This localized tracking deficit creates a clear requirement for computational spatial downscaling architectures that can effectively capture real terrain-wind interactions at sub-kilometer scales without relying on non-existent ground networks or demanding unsustainable computational assets (Höhlein et al., 2020).

Existing downscaling approaches provide various references for grid-scale mismatch resolution. Traditional statistical methods rely heavily on different geostatistical kriging variants, but these methods often do not perform well in reproducing non-linear flow modifications over steep orography (Höhlein et al., 2020). Conversely, convolutional neural networks (CNNs) enable a more powerful extraction of spatial features; previous evaluations show their ability to downscale grid networks from 31 km to 9 km while maintaining correlation scores above 0.8. Other non-linear models reach similar local accuracy. Applications of extreme gradient boosting (XGBoost) across continental mountainous regions resulted in root mean square error (RMSE) scores below 2.0 m/s, while CNN configurations in uniform desert terrains achieved errors below 1.5 m/s (Hu et al., 2023; Zhou et al., 2024).

Withal, these performance baselines are hard to replicate over compressed coastal-mountainous areas where different environmental interfaces meet. Plain convolutional layers suffer from the degradation problem—an optimization bottleneck where accuracy saturates and decays with the increase of network depth, ultimately compromising the capture of micro-scale wind-terrain interactions (Goodfellow et al., 2016). Moreover, a distinct geographic bias limits the direct transferability of existing models. Most existing frameworks were optimized for European mid-latitudes or arid desert settings, and thus are structurally unequipped to handle the strong convective regimes, complicated coastal boundaries and fast land-sea thermal shifts characteristic of equatorial archipelagos (Zhou et al., 2024). Consequently, the modeling of wind fields in these fragmented island environments intrinsically injects a higher level of stochastic noise compared to data-rich continental domains.

To bypass these structural limits, a deep learning architecture based on an encoder-decoder Residual Neural Network (ResNet) variant is proposed to spatially downscale ERA5 wind fields. The deployment of deep residual learning provides clear operational and physical advantages over standard convolutional setups. First, the integration of shortcut skip connections directly counters the degradation and vanishing gradient problems in deep networks, allowing for a more effective characterization of non-linear terrain-wind feedbacks. Second, the network layers capture both localized, micro-scale orographic features and macro-scale regional atmospheric flows simultaneously through residual connections. Lastly, this mechanism accelerates convergence during the training phase, rendering the architecture highly viable for deployment in regions with finite computational infrastructure (Dong et al., 2016; He et al., 2015; Ronneberger et al., 2015).

In this context, a novel spatial downscaling scheme is introduced to downscale coarse ERA5 reanalysis data from a 31-km grid to a 1-km grid over Ambon Island. The proposed approach combines SRTM digital elevation data and regional atmospheric fields using geostatistical kriging and deep residual layers, with local ground measurements strictly dedicated to independent validation. The main contributions of this paper are outlined below:

- The development of an encoder-decoder variant of ResNet specifically tailored for complex coastal-mountainous environments, thereby creating a direct connection between microscale topography and near-surface wind behavior.
- An extensive empirical validation across a range of geographic transition zones (coastal, urban, and marine domains), demonstrating a 54% reduction in Mean Absolute Error (MAE) relative to raw reanalysis data at the highly variable 10-m surface layer.
- A seasonal diagnostic analysis highlighting enhanced model accuracy during monsoon peaks, providing targeted spatial insights for the micro-siting of regional wind farms.
- The delivery of a scalable downscaling pipeline capable of being transferred to other data-sparse, topographically intricate archipelagic environments globally.

The following structure of this manuscript is divided into five main sections. Section 2 describes the multi-channel spatial datasets including the ERA5 reanalysis fields, ground observations and digital elevation models. Section 3 summarizes the methodology including the data preprocessing routines and the proposed deep ResNet downscaling framework architecture. Section 4 presents the assessment of the empirical downscaling results, the ground-station validation metrics, and the spatial comparative profiles.

Finally, Section 5 summarizes the operational conclusions and charts prospective future research trajectories.

2. Data sources

2.1. ERA5 Reanalysis data

The extraction of macro-scale atmospheric fields relies on the ERA5 reanalysis platform (Hersbach et al., 2020), utilizing a ten-year data window spanning from 2013 to 2023. Spatial boundaries are restricted to a specific geographic bounding box over Ambon Island, explicitly defined between the latitudes of 3.25°S–4.0°S and longitudes of 127.75°E–128.5°E. Within this zone, the global dataset operates at a native horizontal grid of about 31 km. The processing pipeline generates hourly near-surface vectors at two distinct vertical levels, 10 m and 100 m above the surface. To construct the final wind speed magnitude at each grid intersection, these raw inputs are systematically broken down into their respective eastward (u) and northward (v) velocity components.

2.2. Ground observation data

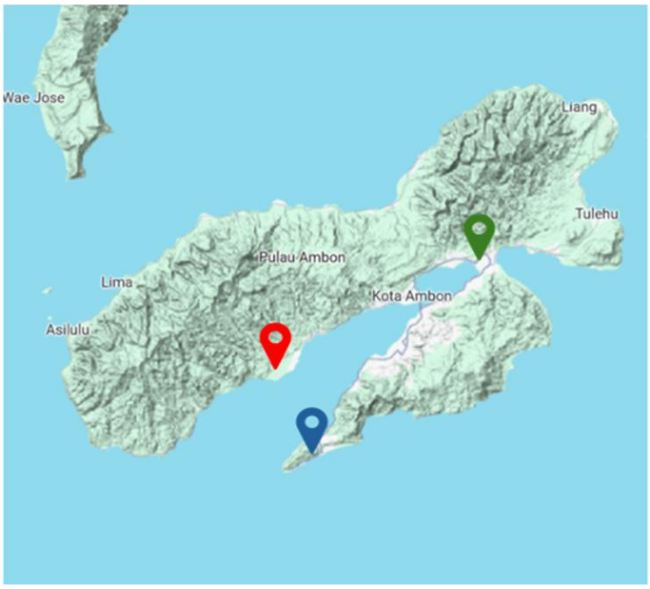

Figure 1. Weather station locations across Ambon Island showing the Meteorological Station (red), Automatic Weather Station (green), and Maritime Weather Station (blue) against topographic background

To empirically validate the results, hourly in-situ data from three weather stations operated by the Indonesian Agency for Meteorology, Climatology and Geophysics (BMKG) are used. Each of these installations is distributed across different landscapes on Ambon Island to sample different boundary layer microclimates, with their exact spatial configurations plotted in Figure 1. The main Meteorological Station on the south coast (3.710°S, 128.08°E; red dot) observes coastal air flows, and the Automatic Weather Station (AWS) at Kota Ambon (3.624°S, 128.247°E; green dot) captures urban canopy interactions. The Maritime Weather Station on the south peninsula (3.790°S, 128.100°E; blue dot) establishes marine flow baselines. All sites measure velocity using anemometers at the standard 10-m reference height and follow specific exposure guidelines within the national monitoring framework.

2.3. Digital Elevation Model (DEM)

Surface morphology configurations were resolved with digital elevation models (DEMs) from the Shuttle Radar Topography Mission (SRTM) at a native spatial resolution of ~30.78 m (Farr et al., 2007). This elevational dataset maps the complex altitudinal gradients of Ambon Island, from sea level to a maximum of 841 m. These topographic matrices are necessary for the calculation of the Terrain Roughness Index (TRI), which is a primary spatial covariate in the downscaling pipeline to account for near-surface flow adjustments over rugged coastal environments.

3. Methodology

The following Figure 2 shows the overall research flowchart.

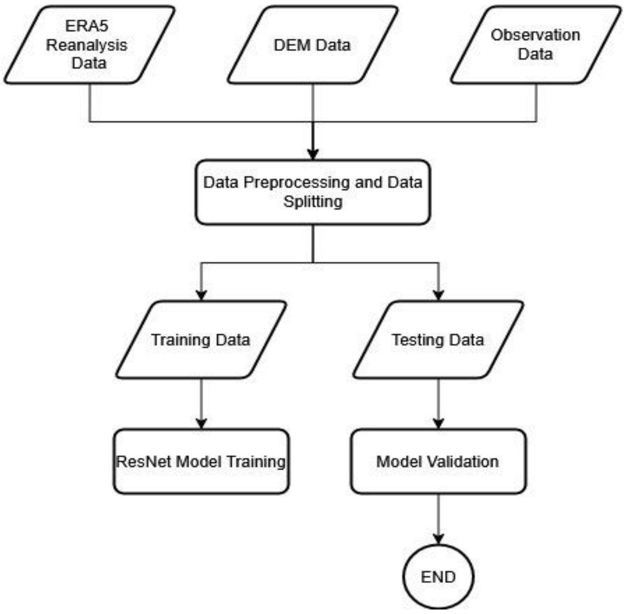

Figure 2. Research Flowchart.

3.1. Data preprocessing

Disparate data streams require systematic structural and temporal harmonization before integration; thus, a multi-tiered preprocessing pipeline is deployed. This pipeline systematically aligns macroscale atmospheric grids, high-resolution topographic matrices, and discrete in-situ observations into a uniform spatial-temporal domain, as conceptualized in the flowchart in Figure 3. The workflow ensures that gridded reanalysis inputs and point-based physical measurements are scale-bridged and numerically stabilized prior to network ingestion.

a. ERA5 data preprocessing

To condition the macroscale atmospheric fields for deep residual mapping, the raw ERA5 reanalysis dataset undergoes a structured, computationally optimized refinement process. First, directional velocity vectors are converted into scalar wind speeds. This transformation resolves the eastward (u) and northward (v) components into a continuous magnitude field, providing a bounded target for the downscaling layers. Second, localized atmospheric anomalies and data corruption are mitigated through statistical quality control. Outliers are flagged using a strict Z-score threshold ($|Z| > 3.0$) and systematically substituted with period-appropriate median values to prevent convective spikes from biasing the training phase.

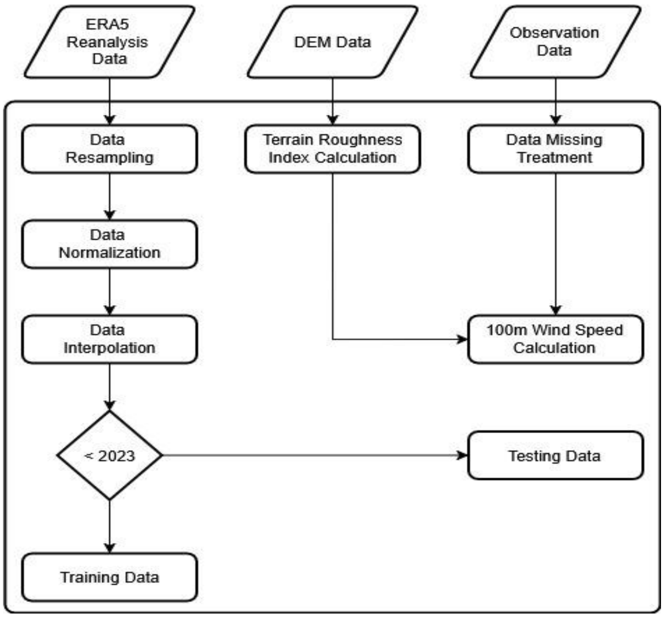

Figure 3. Data Preprocessing Flowchart.

Third, to minimize computational overhead and suppress execution times during the subsequent spatial expansion, numerical stability across deep network transitions is secured preemptively. The scalar inputs are standardized directly on the coarse reanalysis array via min-max normalization according to Eq. (1):

$$X_{norm} = \frac{X - X_{min}}{X_{max} - X_{min}} \quad (1)$$

Normalizing the low-dimensional data prior to spatial expansion significantly reduces matrix calculation costs and ensures that divergent velocity scales do not trigger gradient saturation or explosion during backpropagation. Finally, to bridge the severe resolution gap before deep learning feature extraction, Universal Kriging interpolation utilizing an exponential variogram model is deployed. This geostatistical conditioning disaggregates the normalized coarse 31-km grid into a preliminary 1-km surface matrix according to Eq. (2):

$$Z(S_0) = \sum_{i=1}^{N} \lambda_i Z(S_i) \quad (2)$$

In this formulation, the expression $Z(S_0)$ represents the estimated first-guess value mapped at an unsampled location S_0, whereas $Z(S_i)$ denotes the normalized coarse-grid reanalysis values extracted at surrounding centroids, and λ_i represents the geostatistical weights. To preserve the statistical boundaries necessary for deep learning stability, the post-interpolation matrix is mathematically bounded to the $[0, 1]$ domain, ensuring that minor geostatistical overshoot or undershoot from the Kriging weights does not disrupt network convergence. By incorporating spatial drift driven by regional altitudinal tendencies, this step efficiently supplies the neural network with a structurally conditioned initial-guess field rather than an unaligned coarse array (Wang et al., 2020).

b. Observation data preprocessing

Discrete ground-truth records from the physical weather stations undergo stringent diagnostic screening to patch data gaps and adjust vertical reference frames. Temporal discontinuities are rectified using linear interpolation for brief voids under 6 hours, while moving averages are applied to longer data gaps to maintain climatological consistency. Because engineering-grade resource assessments demand wind speed definitions at modern turbine hub heights, the raw 10-m anemometer measurements must be vertically extrapolated to a 100-m baseline. This vertical shear adjustment is mathematically governed by the logarithmic wind profile law expressed in Eq. (3):

$$V(\mathrm{z}) = V(z_r)\frac{ln\left(\frac{z}{z_r}\right)}{ln\left(\frac{z_r}{z_o}\right)} \tag{3}$$

In this formulation, the term $V(\mathrm{z})$ scales the projected wind velocity at the target 100-m elevation, whereas $V(\mathrm{z_r})$ matches the baseline anemometer readings captured at 10 m. Concurrently, the parameter $V(\mathrm{z_0})$ explicitly quantifies local aerodynamic roughness lengths derived from surface characteristics based on WMO land-use classifications surrounding the station. This formulation accounts for the frictional drag and retarding effects induced by localized coastal-mountainous topographies on vertical boundary layer profiles (Bañuelos-Ruedas et al., 2011), a method extensively validated for wind resource scaling in highly complex maritime terrains (Vu Tuyet & Duong Trung, 2023)

c. DEM Data Preprocessing

Topographic boundary conditions are derived from the SRTM digital elevation dataset to supply the downscaling model with critical sub-grid structural features. Covering Ambon Island's rugged terrain from sea level up to an apex of 841 m, the raw elevation array is rescaled into a uniform 75 × 75 cell matrix to match the exact 1-km target resolution of the downscaled atmospheric fields. In QGIS 3.28, the Terrain Roughness Index (TRI) metric is derived to quantify localized terrain heterogeneity and its blocking effects on near-surface wind vectors. This morphometric operation computes the average elevation difference between a central pixel and its surrounding neighbors within a moving window (Winstral et al., 2017) and produces a static spatial proxy for surface aerodynamic drag.

d. Temporal data partitioning

The operational timeline allocates a ten-year data block spanning from 2013 to 2022 to drive model optimization and network training. In contrast, the subsequent 12 months of 2023 function strictly as an independent verification window to assess model generalizability over full monsoonal cycles. While the atmospheric fields differ over these periods, the static DEM and TRI matrices are fixed, providing a stable boundary condition for the deep learning layers throughout the simulation.

3.2. Proposed downscaling framework

The spatial translation of atmospheric fields from synoptic grids to localized matrices is executed via a modified deep Residual Neural Network (ResNet) topology (He et al., 2016). This deep learning paradigm is specifically engineered to resolve the performance degradation phenomena inherent to standard convolutional layers during backward propagation. By exploiting skip connections, the architecture preserves low-frequency meteorological signals while forcing the intermediate parameters to isolate high-frequency local wind variations driven by steep orographic features. The mathematical abstraction of adaptive residual mapping incorporates domain-specific constraints (Höhlein et al., 2020), formulated in Eq. (4):

$$\mathrm{H}(\mathrm{x}) = \mathrm{F}(\mathrm{x}, \alpha) + \mathrm{G}(\mathrm{x}) \tag{4}$$

where $\mathrm{H}(\mathrm{x})$ represents the target underlying mapping, $\mathrm{F}(\mathrm{x}, \alpha)$ defines the adaptive residual functions parameterized by learning coefficients α and $\mathrm{G}(\mathrm{x})$ symbolizes an enhanced identity operator embedding prior physical boundaries. For the specific task of archipelagic wind field downscaling, this formulation is structurally customized according to Eq. (5):

$$\mathrm{D}(\mathrm{x}) = \mathrm{F}(\mathrm{x}, \mathrm{W}) + \mathrm{I}(\mathrm{x}, \mathrm{T}) \tag{5}$$

wherein $\mathrm{D}(\mathrm{x})$ represents the reconstructed multi-level downscaled wind field tensor, $\mathrm{F}(\mathrm{x}, \mathrm{W})$ denotes the localized residual mapping governed by the trainable weight matrices W and the operator $\mathrm{I}(\mathrm{x}, \mathrm{T})$ functions as an option-conditioned identity link that directly fuses the raw atmospheric matrices with sub-grid topographic inputs T derived from the SRTM-TRI data streams. This architectural integration guarantees that macroscale thermodynamic forces and microscale boundary layer roughness parameters are optimized simultaneously across the network layers.

a. Residual learning principle

The fundamental mechanism driving this framework relies on optimizing residual mappings relative to the input space, bypassing the computational bottlenecks encountered when directly optimizing non-linear objective functions. Given an idealized target mapping $\mathrm{H}(\mathrm{x})$, the stack of convolutional layers is configured to approximate the residual function $F(x) = H(x) - x$. This structure is subsequently reformulated via feedforward pathways into the operational mapping expressed in Eq. (6):

$$H(x) = F(x) + x \tag{6}$$

The mathematical formulation ensures that the identity shortcut connection feeds the unperturbed input information forward across block configurations. Consequently, parameter optimization focuses exclusively on the non-linear perturbation field induced by localized terrain complexities, stabilizing the optimization process and preventing accuracy saturation as network depth increases.

b. Architectural configurations and layer typologies

The structural layout of the specialized downscaling model is partitioned into three cascading functional domains, as depicted in the schematic diagram in Figure 4:

* **Input Processing Topology**: A three-channel spatial tensor consisting of the coarse 10-m wind speeds, 100-m wind fields, and the static digital elevation model (DEM) matrix is ingested by the initialization layer. The feature extraction phase initiates with a 2D convolutional layer (Conv2D) utilizing 64 feature extraction filters, governed by a 3 × 3 spatial kernel, a stride configuration of 1, and 'same' boundary padding. Baseline feature maps are generated by this projection while the initial spatial dimensions of the target domain are fully preserved.

Hierarchical Filter Expansion Blocks: Three sequential residual blocks designed with progressive filter expansion are comprised within the structural core to capture multi-scale atmospheric features. Baseline spatial patterns are mapped by retaining 64 convolutional filters in Residual Block 1. Residual Block 2 expands the channel dimension to 128 filters, and Residual

Block 3 scales up to 256 filters, allowing highly abstract, non-linear interactions between steep orographic slopes and near-surface airflows to be isolated by the deep layers. Each residual block incorporates a pair of convolutional layers utilizing 3×3 kernel dimensions. To accommodate the expanding channel dimensions between blocks, the parallel identity shortcut branches automatically execute 1×1 convolutional projections are automatically executed by the parallel identity shortcut branches, matching the tensor depths structurally before element-wise summation to ensure continuous forward gradient propagation.

* **Decoder Reconstruction Layer**: To re-expand the compressed feature maps into continuous physical grids, a multi-tiered sequence of transposed convolutional operations (Conv2D-Transpose) is employed during the decoding phase. The channel dimensions are systematically disaggregated through a 128-filter and a 64-filter transposed block utilizing 3×3 kernels. The framework terminates at a final (Conv2D) projection layer with 2 output channels, simultaneously yielding the downscaled wind speed arrays at the 10-m and 100-m turbine hub boundaries. A continuous linear activation function is assigned to the terminal layer to handle the unconstrained regression space of localized meteorological predictions. Overfitting risks are mitigated via L_2 weight regularization ($\lambda = 0.001$), while initial parameters are anchored using Kaiming initialization (He et al., 2015) to maintain gradient stability across all hidden nodes.

c. Model optimization and training protocol

Network optimization routines are structured to balance convergence rates and generalization properties, preventing the mathematical network layers from memorizing localized environmental noise.

* **Optimization Parameters and Bounds**: Model weights are updated iteratively via the Adaptive Moment Estimation (Adam) optimizer at a controlled baseline learning rate of 0.0001. To ensure training stability across the steep orographic gradients of Ambon Island, gradient norm clipping is enforced at a threshold of 1.0, whereby exploding gradient anomalies during backpropagation are effectively prevented. The objective minimization function is driven by the Mean Squared Error (MSE) loss metric, wherein large residual deviations are heavily penalized to guarantee high architectural fidelity under extreme monsoonal gust regimes. Numerical constraints are established to include a spatial batch size of 32 configurations, with the total runtime capped at a maximum ceiling of 50 epochs.
* **Overfitting Regularization Strategy**: To guard against over-parameterization in the face of a finite spatial distribution of physical weather stations, an automated early stopping mechanism is integrated into the validation loop. A strict patience parameter of 10 epochs is enforced within the monitoring routine; backpropagation training is automatically ceased if a lower error bound fails to be achieved by the objective validation loss within this window, thereby preserving generalized weight states.
* **Statistical Evaluation Metrics**: Numerical performance evaluation is executed using two complementary metrics: Mean Absolute Error (MAE) and Root Mean Square Error (RMSE). While uniform prediction bias across the target domain is tracked by the MAE, heightened sensitivity to extreme spatial outliers and localized mispredictions is provided by the quadratic scaling of the RMSE (Chai & Draxler, 2014).

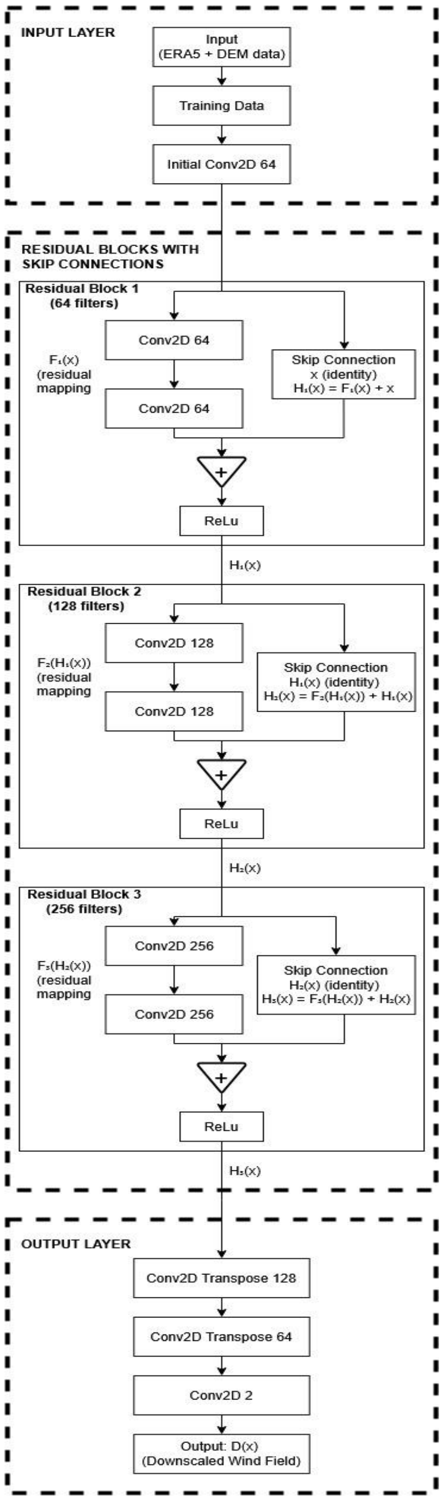

Figure 4. Schematic diagram of the modified ResNet architecture used for wind speed downscaling, showing input layers, residual blocks with skip connections, and output layer.

* **Convergence and Error Profiles**: The model training phase is executed using the historical observational block from 2013 to 2022, while the isolated 2023 monsoonal cycle is utilized strictly for independent testing. Monotonic convergence is confirmed through the empirical monitoring of error trajectories. Due to the preemptive min-max normalization layer a final normalized MAE of 0.0256 and a corresponding normalized RMSE of 0.0475 are achieved within the bounded [0, 1] by the optimized Pytorch pipeline. Computational execution was accelerated utilizing an NVIDIA RTX 3080 hardware infrastructure, establishing an automated, reproducible downscaling framework.

4. Results and discussion

This section presents the performance of our ResNet-based downscaling model on wind speed prediction in Ambon Island, followed by a comprehensive validation against ground observations and comparison with alternative approaches

4.1. Wind field modeling profiles

. The modified deep residual network architecture successfully reconstructs high-resolution continuous wind velocity distributions at both the 10-m near-surface layer and the 100-m turbine hub height boundaries across the complex land-sea interface of Ambon Island. Rather than merely calculating unconstrained climatological means, this assessment isolates specific "feasible energy zones". As visualized in Figure 5, regions with average wind velocities less than the standard turbine cut-in velocity of 4.0 m/s are uniformly masked-out in white, showing possible sites for future microgrid development.

Spatial patterns observed in the 10-m boundary map (Figure 5a) indicate that viable wind development zones at lower altitudes are scarce, appearing as thin strips along the immediate coastal edges. This localized pattern confirms that small-scale wind turbine deployments are still highly limited in inland regions due to rapid loss of kinetic energy from surface roughness friction. Conversely, at the 100-m hub height plane (Figure 5b), the simulated feasible area expands significantly. The model identifies highly distinct, high-potential energy corridors—marked by dark green gradients—extending across the southern and southeastern peninsulas of Leitimur, where localized wind velocities consistently stabilize between 4.5 m/s and 7.5 m/s.

These reconstructed spatial distributions correspond directly to localized macroscale and microscale physical processes. The surface friction drag is at a minimum on the southeastern coast due to the direct and unimpeded exposure to open maritime wind fetches sweeping across the Banda Sea (Y.J. Liu 2024). Whereas, the steep mountain massifs on both sides of the northeastern quadrant impose severe mechanical blocking and thermal stratification effects, forcing the low wind shielding layers observed across the island's interior (Yamaguchi et al., 2024). The stark contrast between the shaded green feasible corridors and the masked white zones demonstrates the deep learning layers' capability to provide high-precision coordinates for microgrid placement.

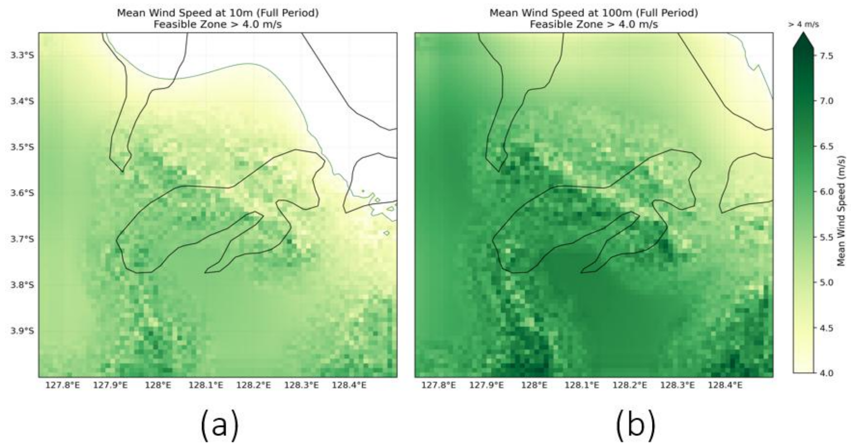

Figure 5. Long-term climatological mean wind speed maps (2013–2023) at (a) 10 m and (b) 100 m heights. The maps isolate the feasible wind energy zones by masking out areas with speeds below the 4 m/s cut-in threshold (white areas). The gradient from yellow to dark green indicates increasing wind potential, revealing key coastal hotspots along the southern peninsula that are viable for wind farm development.

4.2. Ground-station performance validation

Systematic validation procedures are used to evaluate the predictive performance and operational robustness of the deep learning downscaling pipeline by comparing the simulated atmospheric fields with independent in-situ observations. Ground-truth validation datasets are collected at three weather stations operated by the Indonesian Agency for Meteorology, Climatology and Geophysics (BMKG) that are strategically distributed in order to represent the diverse landscapes and abrupt environmental transitions of Ambon Island. The shore-bound Meteorological Station (3.710°S, 128.080°E) documents localized coastal boundary dynamics along the southern margin; the Automatic Weather Station (AWS) (3.624°S, 128.247°E) captures microclimatic wind variations within the municipal structures of Kota Ambon; and the Maritime Weather Station (3.790°S, 128.100°E) tracks unobstructed ocean boundary layers on the southern peninsula. Statistical evaluation utilizes Mean Absolute Error (MAE) and Root Mean Square Error (RMSE). Furthermore, a localized supervised Extreme Gradient Boosting (XGBoost) architecture, trained on an 80% split of the 2023 ground-truth observations, is introduced exclusively at the 10-m near-surface horizontal plane to define the point-specific temporal accuracy baseline. A comprehensive breakdown of the statistical error distributions across all monitoring nodes is compiled in Table 1.

Table 1. Statistical performance comparison. The XGBoost model serves as a supervised benchmark for 10 m predictions.

Station	Height (m)	ResNet MAE (m/s)	XGBoost MAE (m/s)	ResNet RMSE (m/s)	XGBoost RMSE (m/s)
Meteorological	10	2.44	1.16	2.87	1.51
	100	3.06	—	3.65	—
Urban AWS	10	2.78	1.44	3.01	1.90
	100	3.04	—	3.58	—
Maritime	10	2.17	2.67	2.82	3.43
	100	2.25	—	3.10	—

The cross-model benchmarking reveals highly distinct performance trade-offs between local supervised target-fitting and generalized spatial mapping. The point-based supervised XGBoost baseline shows slight error envelopes only at the inland monitoring sites where it was trained directly with historical data, providing the best predictions for the Meteorological station (MAE = 1.16 m/s) and the urban AWS center (MAE = 1.44 m/s). This pattern confirms the capability of supervised algorithms to replicate local point-specific temporal sequences over complex terrains.

However, this localized supervised matching advantage decreases outside its explicit training footprint. Within the open marine zone—the principal geographical target for renewable wind energy infrastructure development—the physics-informed ResNet model outclasses the XGBoost benchmark, achieving a lower MAE (2.17 m/s versus 2.67 m/s) and a superior RMSE trajectory (2.82 m/s versus 3.43 m/s). Such variations exemplify that classical supervised regression optimizes local time series records while the proposed deep learning framework provides better spatial generalization and structural robustness in unobstructed maritime domains.

a. Meteorological station

Continuous temporal tracking at this coastal node exposes clear seasonal variations in network performance across the annual monsoonal cycles, as illustrated in Figure 6. Throughout the active eastern monsoon phase from April to September, the model successfully tracks the temporal progression of regional wind intensities. Simulated near-surface 10-m velocities fluctuate within a 4.0–8.0 m/s band against observed ranges of 3.0–6.5 m/s (Figure 6a), while the 100-m vertical projections map a 9.0–13.0 m/s envelope against ground-truth valuations of 5.0–10.0 m/s (Figure 6b).

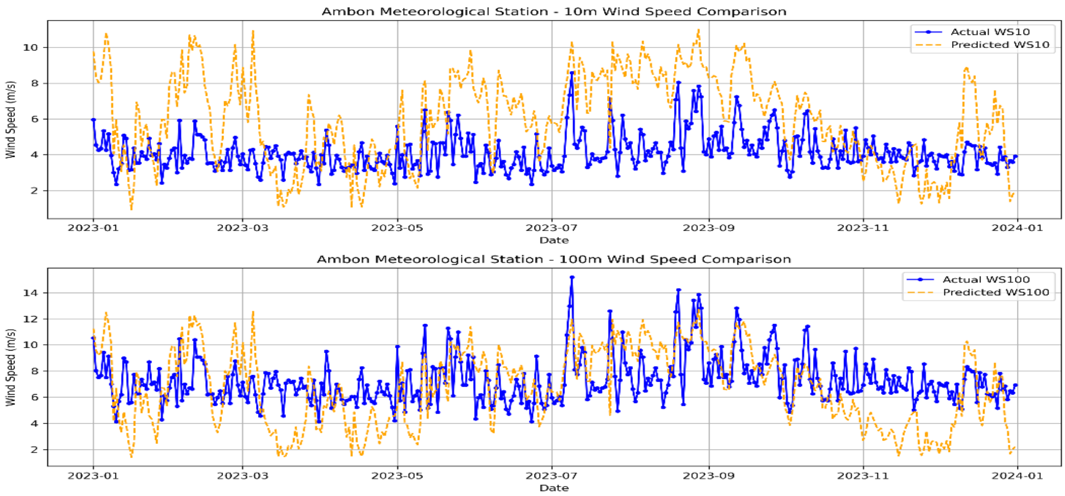

Figure 6. Comparison of predicted versus observed wind speeds at the Meteorological Station during 2023: (a) 10m Wind Speed comparison showing actual (blue solid line) versus predicted (orange dashed line) values, (b) 100m Wind Speed comparison with similar color coding

Time-series monitoring confirms that while the model experiences transient, timestep-specific magnitude discrepancies due to dynamic coastal shoreline boundaries, yielding a baseline 10-m MAE of 2.44 m/s, these variations are distributed symmetrically around the seasonal mean. Deficits become more pronounced at the 100-m elevation, where the vertical uncertainty expands by 25.4%, showing a notable overestimation behavior during peak wind periods from July to September. This systematic drift is due to the interaction between stable regional-scale flow patterns of the Indonesian eastern monsoon system (Aslam et al., 2023) and an insufficient spatial parameterization of local vegetation dynamics along the southeastern sector, where complex canopy-atmosphere interactions induce severe mechanical turbulence and velocity friction layers that escape regional topographically driven terrain approximations (Brunet, 2020).

b. Automatic Weather Station

On the other hand, the municipal AWS coordinate is subject to high error configurations, characterized by a persistent positive overestimation shift throughout the entire annual cycle, as shown in Figure 7. Statistical log analysis reveals systematic overestimation rates of 13.8% at the 10-m boundary layer and 18.2% at the 100-m turbine hub plane. While physical urban observations remain heavily suppressed below 2.5 m/s due to building shelter effects, the downscaled simulations generate fluctuating trends between 2.0 m/s and 6.0 m/s at the 10-m line, which further expands to a 5.0–10.0 m/s band at the 100-m level.

Such structural discrepancies emphasize the inherent complexity of resolving urban boundary layers. Within these municipal zones, clustered architectural arrangements disrupt macroscale wind trajectories by introducing localized frictional drag and turbulent obstacle wakes (McKenna et al., 2022). In fact, built-up environments routinely attenuate ambient wind velocities by 20% to 30% compared to unobstructed fields. This localized deceleration phenomenon is heavily driven by elevated surface aerodynamic roughness and the unique formulation of distinct microclimatic canopy sub-layers (Reja et al., 2022).

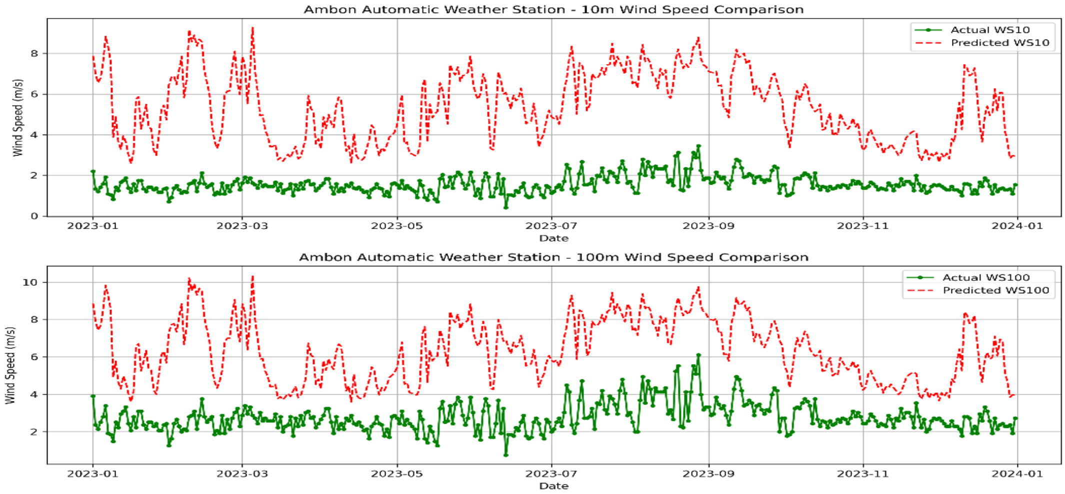

Figure 7. AWS wind speed comparison showing predicted versus observed values: (a) 10m Wind Speed comparison with actual values (green solid line) consistently lower than predicted values (red dashed line), (b) 100m Wind Speed comparison showing similar systematic.

Since the model does not explicitly incorporate building footprint and building height parameters, the network interprets the dense urban core as an open valley floor with no obstructions, resulting in unattenuated velocity projections.

c. Maritime weather station

The open maritime boundary layer at this station produces the most stable, robust validation profiles during the mid-year eastern monsoonal flow from April to September (Figure 8). This improved predictive tracking is due to the node's optimal exposure to unperturbed maritime wind streams and the relative aerodynamic homogeneity of sea surfaces.

Simulated near-surface trends closely overlap ground-truth readings (Figure 8a), maintaining excellent temporal synchronization across the 10-m vertical hub plane during peak velocity regimes (Figure 8b). The 10-m marine validation records a highly optimized error profile with an MAE of 2.17 m/s.

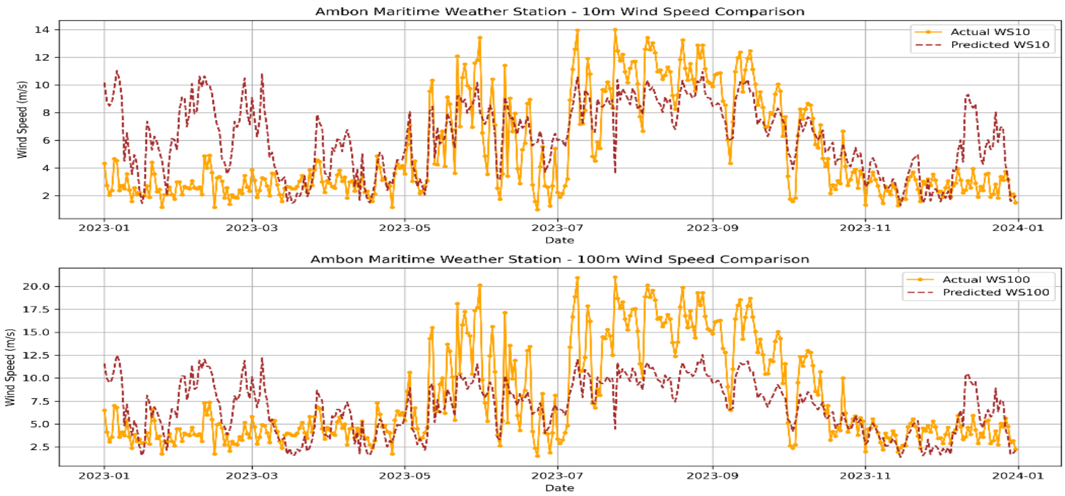

Figure 8. Maritime Weather Station comparison showing predicted versus observed values: (a) 10m Wind Speed comparison with actual values (orange solid line) and predicted values (brown dashed line) showing good correlation, particularly during eastern monsoon periods (April to September), (b) 100m Wind Speed comparison demonstrating similar synchronization between observed and predicted patterns.

Statistical checks confirm this clean modeling profile. At this specific coordinate, the residual error fields satisfy the Shapiro-Wilk normality criteria ($p > 0.05$). This mathematical distribution suggests that localized variance is mainly random stochastic noise rather than a deep systematic drift. This is consistent with the low aerodynamic roughness and steady land-sea wind circulation typical of marine environments (Y.J. Liu 2024). The network also has a large temporal response during the seasonal transition from October to November, capturing the rapid drops in wind intensity due to the change of monsoonal phases. The architecture manifests its core ability to represent non-stationary atmospheric variations during these rapid seasonal drops. The forecast accuracy, however, decreases during the long western monsoonal period from October to March, where the transient weather systems and complex land-sea thermal interactions pose further challenges for the simulation.

4.3. Comparative analysis

A comprehensive spatial comparison of long-term mean wind speed distributions spanning the multi-decadal block (2014–2023) is illustrated in Figure 9, highlighting the distinct structural variations captured by three independent mapping methodologies. The side-by-side visualization maps horizontal profiles at both the near-surface 10-m boundary line (left panels) and the 100-m turbine hub height elevation (right panels), revealing severe resolution discrepancies and pattern representation limits across the evaluated frameworks.

The raw ERA5 reanalysis dataset (Figure 9a) exhibits critical spatial resolution constraints across the island's narrow boundaries. Due to the rigid nature of its native grid cells (~31 km), simulated velocities are restricted to an over-smoothed 2.7–5.4 m/s range at the 10-m line, increasing only marginally to a 3.0–5.4 m/s band at the 100-m hub height level. This low-resolution grid is mathematically unable to capture the compressed topographical features of Ambon Island, resulting in uniform color fields along coastal-inland transition zones where the absence of realistic gradients fails to simulate localized aerodynamic flow modifications.

Universal Kriging interpolation (Figure 9b) delivers improved spatial grid refinement compared to raw reanalysis fields, projecting a much smoother wind field expansion across the landmass. Nonetheless, this geostatistical alternative displays inherent limits in resolving genuine wind-terrain physical interactions. Because the variogram model functions purely on statistical distance weightings, it generates gradual transitions that lack the high-frequency localized wind speed variations necessary to capture complex microclimatic blocking or coastal airflow enhancements.

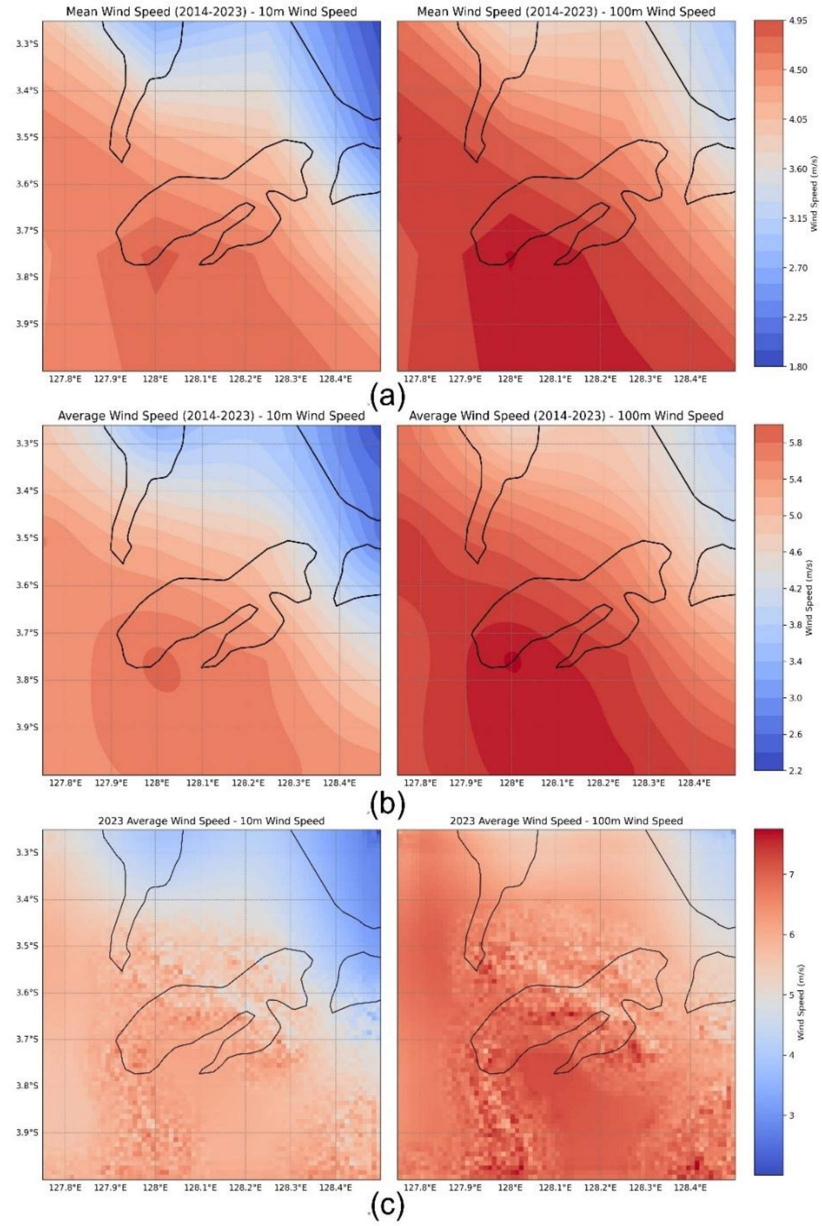

Figure 9. Visual comparison of long-term mean wind speeds (2014–2023) derived from: (a) coarse-resolution ERA5 reanalysis, (b) Universal Kriging interpolation, and (c) the proposed ResNet model. The ResNet output reveals fine-grained spatial details and localized high-wind zones (right panel) that are otherwise smoothed out in the ERA5 and Kriging baselines.

In contrast, the proposed deep learning framework (Figure 9c) demonstrates superior capability in reconstructing fine-scale spatial layouts while maintaining meteorological consistency across the domain. The model successfully resolves detailed velocity gradients triggered by Ambon's rugged mountain terrain. Enhanced pixel resolution is particularly evident along the shorelines where sharp land-sea wind transitions occur, alongside high elevated ridges where localized orographic flow accelerations are accurately mapped. This detailed layout exposes sharp local velocity gradients that are completely lost within both the ERA5 and Kriging baselines. To supplement this spatial analysis, a quantitative tracking of validation error profiles across all physical monitoring nodes is summarized in Table 2.

Quantitative validation values confirm substantial error reductions at the coastal and marine monitoring sites. At the Maritime weather station, the proposed ResNet network achieves a 54% reduction in MAE (dropping from 4.71 m/s to 2.17 m/s) and a 51% reduction in RMSE (dropping from 5.79 m/s to 2.82 m/s) compared to baseline benchmarks. Conversely, a localized performance inversion occurs at the urban AWS coordinate. At this specific inland node, both the ERA5 input and the geostatistical Kriging baseline record tighter error boundaries (MAE = 1.08 m/s, R^2 = 0.73) than the deep learning architecture.

Table 2. Comparison of Validation Metrics Across Different Methods

Station Node	Downscaling Methodology	MAE (m/s)	RMSE (m/s)	Coefficient of Determination (R2)
Meteorological	Raw ERA5 Reanalysis (~31 km)	3.63	3.76	0.62
	Universal Kriging Interpolation	5.28	5.45	0.53
	Proposed ResNet Architecture	2.44	2.87	0.78
AWS	Raw ERA5 Reanalysis (~31 km)	1.08	1.15	0.73
	Universal Kriging Interpolation	1.08	1.15	0.73
	Proposed ResNet Architecture	2.78	3.01	0.65
Maritime	Raw ERA5 Reanalysis (~31 km)	4.71	5.79	0.59
	Universal Kriging Interpolation	6.78	8.28	0.41
	Proposed ResNet Architecture	2.17	2.82	0.84

This unique trend does not indicate a superior representation of boundary layer physics, but operates as an artifact of spatial smoothing. Because the municipal AWS node is centered within a wide, low-lying inland valley structure, the linear interpolation properties of the Kriging variogram create an artificially smooth, low-velocity field. This localized per-grid relaxation happens to mathematically coincide with the heavily sheltered urban observations. Furthermore, the identical error profiles between raw ERA5 and Kriging at this specific node indicate that the AWS coordinate falls entirely within a single dominant, low-variance native ERA5 grid cell, which structurally binds the geostatistical interpolation to the raw reanalysis baseline. In contrast, the ResNet model encounters simulation challenges due to the highly non-linear wind patterns within the urban core, combined with the lack of explicit sub-grid building footprint arrays.

When evaluated against global deep learning achievements, the domain-wide composite model RMSE stands higher than equivalent downscaling implementations trained across flat, continental sectors. Prior networks report tighter global error boundaries, including wind simulations over Germany where RMSE equals 1.64 m/s (Höhlein et al., 2020), cross-border Central European zones with an RMSE of 2.05 m/s (Hu et al., 2023), and the uniform surface layers of the Tengger Desert yielding an RMSE of 1.89 m/s (Zhou et al., 2024).

This performance gap highlights the intense challenges of archipelagic wind modeling. Continental study areas feature broad plains with uniform roughness scales, allowing neural networks to converge smoothly during backpropagation. In contrast, Ambon Island represents a highly compressed topography characterized by extreme elevation shifts over very short horizontal distances. The close convergence of coastal boundaries, rugged mountain massifs (such as the Leitimur and Hitu ridges), and dense urban centers generates high localized turbulence and microclimatic variance. This intense sub-grid spatial variance introduces significant irreducible uncertainty, demonstrating that deep learning frameworks optimized for continental zones require region-specific orographic training and coastal boundary weightings to effectively manage complex island microclimates.

4.4. Research limitations and future outlook

The proposed modified ResNet framework is able to reconstruct fine-scale wind fields over the archipelagic terrain of Ambon Island with good ability, but it still has several structural and physical limitations. A primary architectural constraint stems from the complete omission of explicit three-dimensional building footprints and municipal displacement heights within the input layers. As documented in the urban AWS validation metrics, the neural network tends to misinterpret densely built environments as unobstructed valley floors. The model is unable to resolve localized friction channeling, structural wake formations and the strong wind speed attenuation characteristic of the municipal canopy layers due to the absence of sub-grid urban parameterization. To fill these gaps in the urban boundary layer, the systematic integration of Urban Canopy Models (UCM) or high-resolution surface roughness matrices derived from satellite-based light detection and ranging (LiDAR) datasets should be considered in future network iterations.

Another physical limitation arises from the static representation of surface aerodynamic properties over densely vegetated areas. The observed systemic overestimation at the 100-m plane of the coastal Meteorological station during peak monsoonal periods highlights the difficulty in modeling complex canopy-atmosphere interactions. The current framework uses the static Terrain Roughness Index (TRI) to estimate surface friction profiles, which does not account for seasonal vegetation dynamics, changes in foliage density and wind-induced canopy turbulence. To resolve these localized mechanical disturbances, future deep learning architectures should incorporate time-varying biogeophysical parameters, such as the Leaf Area Index (LAI) or Normalized Difference Vegetation Index (NDVI), to introduce dynamic friction boundaries into the downscaling process.

Furthermore, the predictive accuracy assessment of the model is constrained by spatial data scarcity, a common challenge in tropical archipelagic regions. While the network utilizes continuous gridded reanalysis fields for training, the sparse spatial distribution and limited density of the ground-truth BMKG weather station network restrict the number of high-fidelity observation nodes available for independent spatial verification and regional weight fine-tuning. This localized observational scarcity introduces higher aleatoric uncertainty when establishing point-specific error convergence compared to continental downscaling initiatives that benefit from dense, highly interconnected observational arrays.

Finally, the model currently operates on a decoupled spatial-temporal training routine optimized for daily averages. While this configuration successfully captures large-scale monsoonal shifts, it smooths out sub-hourly convective wind gusts and transient microclimatic transitions. Future work will focus on developing fully coupled spatiotemporal neural network architectures, such as integrating Convolutional Long Short-Term Memory (ConvLSTM) layers with deep residual blocks. Moreover, the incorporation of secondary atmospheric variables such as Sea Surface Temperature (SST), convective indices and relative humidity fields in the input feature space would greatly enhance the forecasting capabilities of the model during volatile, non-stationary inter-monsoonal transition windows.

5. Conclusion

The emergence of deep learning downscaling models has provided a remarkable advancement to the predictive understanding of localized wind patterns over complex coastal-mountainous terrains. The employed deep residual framework demonstrates a high-fidelity reproduction of fine spatial-temporal wind fields over the compressed geography of Ambon Island. Most notably, the network reaches impressive optimization in maritime boundary layers, with localized MAE (Mean Absolute Error) levels of 2.17 m/s at the 10-m surface level and 2.25 m/s at the 100-m vertical turbine hub height. These predictive outputs represent a major structural enhancement over traditional geostatistical interpolation routines, particularly in resolving the sub-grid atmospheric configurations essential for high-fidelity wind resource assessments.

Systematic validation routines reveal distinct performance behavior across contrasting land-use settings and topographic environments. The open maritime areas were found to provide the most consistent and reliable historical synchronization, while the built-up urban areas were found to have acute parameterization challenges. A persistent positive displacement is found within the urban boundaries, with systematic wind velocity overestimation of 13.8% at the 10-m level and 18.2% along the 100-m hub plane. This vertical discrepancy highlights the significant atmospheric impact of localized building shelter conditions and unresolved surface aerodynamic roughness boundaries on downscaling performance. Seasonal assessments further validate superior predictive coherence during the active eastern monsoon phase (April to September), despite a subtle mathematical tendency toward velocity overestimation during peak regional wind sequences.

The quantitative results of this study contribute several key insights to renewable energy modeling. The production of high-resolution microclimatic wind maps at both 10-m and 100-m elevations, by identifying specific "feasible energy zones", provides a robust empirical basis for future microgrid development and long-term infrastructure planning along Ambon's high-potential coastal corridors. At the same time, the exhaustive multi-node validation protocol establishes a stringent framework for assessing neural downscaling models in highly complex island ecosystems. The underlying downscaling methodology maintains generic scientific validity, enabling future adaptation across topographically challenging archipelagic zones where dynamic maritime interfaces and steep terrain gradients generate non-stationary atmospheric variations.

Acknowledgements

Author Contributions: All authors have read and agreed to the published version of the manuscript.
Conflicts of Interest: The authors declare no conflict of interest.

References

Ángel-Sanint, E., García-Orrego, S., & Ortega, S. (2023). Refining wind and solar potential maps through spatial multicriteria assessment. Case study: Colombia. *Energy for Sustainable Development*. https://doi.org/10.1016/j.esd.2023.01.019

Aslam, A. A., Schwendike, J., Peatman, S. C., Birch, C. E., Bollasina, M. A., & Barrett, P. (2023). Mid-level dry air intrusions over the southern Maritime Continen. *Quarterly Journal of the Royal Meteorological Society*, *150*(759), 727-745. https://doi.org/https://doi.org/10.1002/qj.4618

Bañuelos-Ruedas, F., Ángeles Camacho, C., & Rios-Marcuello, S. (2011). Methodologies Used in the Extrapolation of Wind Speed Data at Different Heights and Its Impact in the Wind Energy Resource Assessment in a Region. In *InTech*.

Brunet, Y. (2020). Turbulent Flow in Plant Canopies: Historical Perspective and Overview. *Boundary-Layer Meteorology*. https://doi.org/https://doi.org/10.1007/s10546-020-00560-7

Cendrawati, D., Hesty, N., Pranoto, B., Aminuddin, A., Kuncoro, A., & Fudholi, A. (2023). Short-Term Wind Energy Resource Prediction Using Weather Research Forecasting Model for a Location in Indonesia. *International Journal of Technology*, *14*, 584. https://doi.org/10.14716/ijtech.v14i3.5803

Chai, T., & Draxler, R. R. (2014). Root mean square error (RMSE) or mean absolute error (MAE)? – Arguments against avoiding RMSE in the literature. *Geoscientific Model Development*. https://doi.org/10.5194/gmd-7-1247-2014

Deng, Y. Y., Haigh, M., Pouwels, W., Ramaekers, L., Brandsma, R., Schimschar, S., Grözinger, J., & de Jager, D. (2015). Quantifying a realistic, worldwide wind and solar electricity supply. *Global Environmental Change*, *31*, 239-252. https://doi.org/https://doi.org/10.1016/j.gloenvcha.2015.01.005

Dong, C., Loy, C. C., He, K., & Tang, X. (2016). Image Super-Resolution Using Deep Convolutional Networks. *IEEE Transactions on Pattern Analysis and Machine Intelligence*, *38*(2), 295-307. https://doi.org/10.1109/TPAMI.2015.2439281

Farr, T. G., Rosen, P., Caro, E., Crippen, R., Duren, R., Hensley, S., Kobrick, M., Paller, M., Rodriguez, E., Roth, L., Seal, D., Shaffer, S., Shimada, J., Umland, J., Werner, M., Oskin, M., Burbank, D., & Alsdorf, D. (2007). The Shuttle Radar Topography Mission. *Reviews of Geophysics*. https://doi.org/10.1029/2005RG000183

Goodfellow, I., Bengio, Y., & Courville, A. (2016). *Deep Learning*. MIT Press. https://www.deeplearningbook.org/

He, K., Zhang, X., Ren, S., & Sun, J. (2015, 7-13 Dec. 2015). Delving Deep into Rectifiers: Surpassing Human-Level Performance on ImageNet Classification. 2015 IEEE International Conference on Computer Vision (ICCV),

He, K., Zhang, X., Ren, S., & Sun, J. (2016). Deep Residual Learning for Image Recognition.

Hersbach, H., Bell, B., Berrisford, P., Hirahara, S., Horányi, A., Muñoz-Sabater, J., Nicolas, J., Peubey, C., Radu, R., Schepers, D., Simmons, A., Soci, C., Abdalla, S., Abellan, X., Balsamo, G., Bechtold, P., Biavati, G., Bidlot, J., Bonavita, M.,…Thépaut, J.-N. (2020). The ERA5 global reanalysis. *Quarterly Journal of the Royal Meteorological Society*. https://doi.org/10.1002/qj.3803

Höhlein, K., Kern, M., Hewson, T., & Westermann, R. (2020). A comparative study of convolutional neural network models for wind field downscaling. *Meteorological Applications*. https://doi.org/10.1002/met.1961

Hu, W., Scholz, Y., Yeligeti, M., von Bremen, L., & Deng, Y. (2023). Downscaling ERA5 wind speed data: a machine learning approach considering topographic influences. *Environmental Research Letters*. https://doi.org/10.1088/1748-9326/aceb0a

Kalverla, P. C., Duncan, J. B., Jr., Steeneveld, G.-J., & Holtslag, A. A. M. (2019). Low-level jets over the North Sea based on ERA5 and observations: together they do better. *Wind Energ. Sci.* https://doi.org/10.5194/wes-4-193-2019

Langer, J., Simanjuntak, S., Pfenninger, S., Laguna, A. J., Lavidas, G., Polinder, H., Quist, J., Rahayu, H. P., & Blok, K. (2022). How offshore wind could become economically attractive in low-resource regions like Indonesia. *iScience*, *25*(9), 104945. https://doi.org/https://doi.org/10.1016/j.isci.2022.104945

Luo, W., Taylor, M. C., & Parker, S. R. (2008). A comparison of spatial interpolation methods to estimate continuous wind speed surfaces using irregularly distributed data from England and Wales. *International Journal of Climatology*, *28*(7), 947-959. https://doi.org/https://doi.org/10.1002/joc.1583

McKenna, R., Pfenninger, S., Heinrichs, H., Schmidt, J., Staffell, I., Bauer, C., Gruber, K., Hahmann, A. N., Jansen, M., Klingler, M., Landwehr, N., Larsén, X. G., Lilliestam, J., Pickering, B., Robinius, M., Tröndle, T., Turkovska, O., Wehrle, S., Weinand, J. M., & Wohland, J. (2022). High-resolution large-scale onshore wind energy assessments: A review of potential definitions, methodologies and future research needs. *Renewable Energy*, *182*, 659-684. https://doi.org/https://doi.org/10.1016/j.renene.2021.10.027

Nunumete, R. (2015). ANALYSIS OF WIND POWER POTENTIAL IN AMBON ISLAND, INDONESIA. *Alternative Energy and Ecology (ISJAEE)*, 26-32. https://doi.org/10.15518/isjaee.2015.01.002

Pambudi, N. A., Firdaus, R. A., Rizkiana, R., Ulfa, D. K., Salsabila, M. S., Suharno, & Sukatiman. (2023). Renewable Energy in Indonesia: Current Status, Potential, and Future Development. *Sustainability*, *15*(3).

Pelupessy, D., & Manuhutu, F. (2019). Hybrid solar-wind-diesel power plant for small islands in Maluku Province. *IOP Conference Series: Earth and Environmental Science*, *339*(1), 012046. https://doi.org/10.1088/1755-1315/339/1/012046

Reja, R. K., Amin, R., Tasneem, Z., Ali, M. F., Islam, M. R., Saha, D. K., Badal, F. R., Ahamed, M. H., Moyeen, S. I., & Das, S. K. (2022). A review of the evaluation of urban wind resources: challenges and perspectives. *Energy and Buildings*, *257*, 111781. https://doi.org/https://doi.org/10.1016/j.enbuild.2021.111781

Ronneberger, O., Fischer, P., & Brox, T. (2015, 2015//). U-Net: Convolutional Networks for Biomedical Image Segmentation. Medical Image Computing and Computer-Assisted Intervention – MICCAI 2015, Cham.

Shafira, A. N., Petrana, S., Muthia, R., & Purwanto, W. (2023). Techno-economic analysis of a hybrid renewable energy system integrated with productive activities in an underdeveloped rural region of eastern Indonesia. *Clean Energy*, *7*, 1247-1267. https://doi.org/10.1093/ce/zkad068

Sørensen, P., Litong-Palima, M., Hahmann, A. N., Heunis, S., Ntusi, M., & Hansen, J. C. (2018). Wind power variability and power system reserves in South Africa. *Journal of Energy in Southern Africa*. https://doi.org/10.17159/2413-3051/2017/v29i1a2067

Statistics, C. B. o. (2024). *AMBON MUNICIPALITY IN FIGURES 2024*. Ambon, Indonesia: BPS-Statistics of Ambon Municipality

Veronesi, F., Grassi, S., & Raubal, M. (2016). Statistical learning approach for wind resource assessment. *Renewable and Sustainable Energy Reviews*, *56*, 836-850. https://doi.org/https://doi.org/10.1016/j.rser.2015.11.099

Vu Tuyet, C., & Duong Trung, K. (2023). Evaluation of wind energy potential: A case study in Vietnam. 2023 Asia Meeting on Environment and Electrical Engineering (EEE-AM), Hanoi, Vietnam.

Wang, Y., Wang, D., Zhao, J., & Zhu, C. (2020). Wind speed spatial estimation using geostatistical kriging. *IOP Conference Series: Earth and Environmental Science*, *619*(1), 012049. https://doi.org/10.1088/1755-1315/619/1/012049

Winstral, A., Jonas, T., & Helbig, N. (2017). Statistical Downscaling of Gridded Wind Speed Data Using Local Topography. *Journal of Hydrometeorology*, *18*(2), 335-348. https://doi.org/10.1175/JHM-D-16-0054.1

Y.J. Liu , Y. C. H., Y.H. He , Y.H. Liu , J.Y. Fu (2024). Influence of turbulence intensity on wind effects toward a high-rise building with curved cross-section at coastal area. *Journal of Wind Engineering and Industrial Aerodynamics*, *253*.

Yamaguchi, A., Tavana, A., & Ishihara, T. (2024). Assessment of Wind over Complex Terrain Considering the Effects of Topography, Atmospheric Stability and Turbine Wakes. *Atmosphere*, *15*(6).

Zhou, H., Luo, Q., & Yuan, L. (2024). Downscaling and Wind Resource Assessment of Climatic Wind Speed Data Based on Deep Learning: A Case Study of the Tengger Desert Wind Farm. *Atmosphere*. https://doi.org/10.3390/atmos15030271